ACS OMEGA

http://pubs.acs.org/journal/acsodf

Article

Contact Enhancement in Nanoparticle Assemblies through Electrophoretic Deposition

Yoonsu Park, Wooseok Jeong, Junhyuk Ahn, Yun-Kun Hong, Eunseo Hwang, Minyoung Kim, Yun Jae Hwang, Soong Ju Oh, and Don-Hyung Ha*

Cite This: *ACS Omega* 2022, 7, 41021−41032

Read Online

ACCESS | Metrics & More | Article Recommendations | Supporting Information

ABSTRACT: A strong interparticle connection needs to be realized to harvest unique nanoscale features of colloidal nanoparticles (NPs) in film structures. Constructing a strong contact and adhesion of NPs on a substrate is an essential process for improved NP film properties, and therefore, its key factors should be determined by understanding the NP deposition mechanism. Herein, we investigated the critical factors leading to the robust and strong adherence of the film structure and revealed that the NP deposition mechanism involved the role of surfactant ligands during electrophoretic deposition (EPD). The high amount of surfactant ligand treatment results in a high deposition rate of NPs in the early stage; however, the ligand treatment does not influence the deposition rate in the later stage. Furthermore, the deposition mechanism is found to involve three steps during EPD: island formation, lateral growth, and layer-by-layer deposition. Rapid NP deposition kinetics controlled by ligand treatments demonstrate the strong contact and adhesion of NP film structures; they are characterized by the fast charge transfer, low resistivity, and rigid NP layers of the $Cu_{2-x}S$ NP-based devices. Finally, the controlled role of surfactant ligands in EPD enables design of high-performance nanostructured NP film devices with contact enhancement.

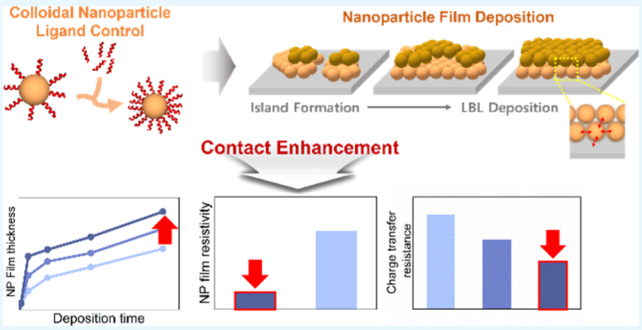

1. INTRODUCTION

Unlike bulk materials, nanoparticles (NPs) exhibit unique electrical, optical, mechanical, and chemical properties, which suggests the potential for use in a wide range of applications.[1,2] Solution-based colloidal synthesis procedures have been widely used in the design of uniformly sized metallic, semiconducting, and insulating NPs with various shapes and compositions.[3,4] Colloidal NPs provide unique properties for various materials that cannot be achieved in the traditional bulk structure, and therefore, it is highlighted as a building block for nanostructured devices.[5,6] Solution-based processes such as spin-coating, dip-coasting, spray-coating, drop-casting, and inject-printing are used to fabricate nanostructured films from colloidal NPs.[7−10] The strategy used to assemble individual NPs for maximizing the properties of colloidal NPs as devices is controlled by multiple physical contacts between NPs and the substrate, the orientation of NPs on a substrate, and the fabrication of a strong adhesive film format.[8,11,12] However, the large-scale formation of high-density and crack-free film structures continues to remain a challenge in conventional fabrication processes.[13,14]

Recently, electrophoretic deposition (EPD) has emerged as an alternative method for building colloidal NP films through a simple equipment configuration.[15] The moving species for EPD are solid particles, and they can be easily adapted to various materials such as metals, ceramics, polymers, and biomolecules; furthermore, they can be selected as a target particle without any chemical reaction on the substrate/NP interface.[16] The advantages of EPD include strong adherence between the particles and the conductive substrate with a high density coating, applicability over a wide range of substrate shapes, possibility of the selective deposition of particles for the desired area, no vacuum process, and no high temperature requirement, which are difficult to achieve using other conventional manufacturing methods.[13,17] Nanostructured films fabricated through EPD have been widely applied to various applications such as water-splitting electrocatalysts,[18] quantum dot light-emitting diodes,[19] battery electrodes,[20] solar cells,[21] and screen panels;[22] they show enhanced performances compared to those of the devices fabricated using traditional techniques.

Based on the classical EPD theory, the number of particles to be deposited on the electrode can be expressed using the Hamaker equation as

Received: July 11, 2022
Accepted: September 9, 2022
Published: November 1, 2022

https://doi.org/10.1021/acsomega.2c04366
ACS Omega 2022, 7, 41021−41032

$$W = \frac{3}{2} C\varepsilon_0\varepsilon_r\xi\left(\frac{1}{\eta}\right)\left(\frac{E}{L}\right)t \quad (1)$$

eq 1 indicates that the particle amount deposited per unit area of electrode (W) is directly related to the concentration of the solution (C), applied voltage (E), deposition time (t), vacuum permittivity(ε_0), dielectric constant of the solvent (ε_r), zeta potential (ξ), viscosity of the solvent (η), and distance between the two electrodes facing each other (L). Currently, the advanced kinetic models of the EPD process using colloidal NPs are established based on this Hamaker equation.[23] The film thickness and morphology of the EPD product can be easily controlled through NP concentrations, deposition voltages, and deposition times. The NP solution-related factor can be derived using the electrophoretic mobility (μ) equation[24] given as

$$\mu = \frac{\nu}{E} = \frac{2}{3}\frac{\varepsilon_0\varepsilon_r\xi}{\eta} f(\kappa r) \quad (2)$$

The electrophoretic mobility equation represents the velocity of moving particles (ν) when an electric field (E) is applied to the charged particle; $f(\kappa r)$ represents the Henry coefficient. eq 2 indicates that the relative surface charge intensity of colloidal NPs, represented by the zeta potential, is related to the electrophoretic mobility. In other words, the particle's moving behavior under an electric field is dominated by the charge states of the particles based on eq 2. The surface charge state of colloidal NPs can be controlled by experimental procedures involving surfactant ligands, which can determine particle movement toward the charged electrode during EPD.

The net charge of NPs dispersed in non-polar solvents such as hexane or chloroform depends on the coverage of the surfactant ligand that can be effectively controlled by the partial removal of the ligand or the addition of excess ligands through a precipitation step of colloidal NPs.[25−27] Islam et al. reported a correlation between the controlled ligand coverage by the precipitation step and the morphology of the NP film formed by EPD with CdSe NPs dispersed in hexane.[28] The optimization of surfactant ligand coverages is the key to fabricating high-quality NP films via EPD. Jia et al. reported that the physical properties of colloidal NPs significantly depend on the amount of ligands, which result in the electrophoretic mobility change.[29] Singh et al. demonstrated that influence of the net charge on CdSe nanorod assembly formation.[30] The vertical alignment and random orientation of the nanorod were selectively implemented through the ligand exchange. In addition, Oberdick et al. also demonstrated the electric field-driven nucleation of the spherical iron oxide NP assemblies through the EPD.[31] However, unlike the theoretical and experimental reports, the NP deposition mechanism under the electric field during EPD, which is affected by organic ligands, is still poorly understood. Previously, our group reported that the solvent and surfactant ligands of copper sulfide ($Cu_{2-x}S$) and iron oxide NPs are key factors influencing the NP deposition behavior and film morphology of the EPD system.[32−34]

In this study, we systematically investigate the critical factors for fabrication of strongly attached NP film structures through understanding the NP deposition mechanism during EPD. Different deposition phenomena of the $Cu_{2-x}S$ NPs were dominated by various surfactant ligand treatment amounts, which indicate that controlling the ligand amount is effective for achieving NP charge conversion, improved deposition kinetics, NP film growth mechanism, and deposition of the uniform NP film. In all EPD experiments, rapid NP deposition kinetics are indicative of a high initial current during EPD. The ligand treatment amounts influence the control of the NP deposition rates at the initial EPD stage; however, they had negligible effect on the following stage. Furthermore, the fast charge transfer and low resistivity properties of the rigid NP film structures, which could be attributed to the high adhesion of the NPs to the substrate, were achieved from the optimized EPD with the ligand-treated NPs. Uncovering the role of surfactant ligands in the colloidal NP deposition provides a facile route for the kinetic control of NP deposition and the fabrication of high-performance nanostructured NP film devices.

2. EXPERIMENTAL SECTION

2.1. Chemicals and Materials. Copper (II) chloride dihydrate ($CuCl_2{\cdot}2H_2O$, ≥99%, ACS Reagent), di(*tert*-butyl) disulfide (TBDS, 97%), and oleylamine (OLA, 70%, technical grade) were purchased from Sigma-Aldrich. Acetone (99.5%, extra pure) and *n*-hexane (95%, extra pure) were purchased from Daejung Chemicals and Metals. Methanol (99.5%) was purchased from Samchun Chemical. Sodium sulfide (Na_2S) anhydrous was purchased from Alfa Aesar. All the chemicals were used without further purification.

2.2. Synthesis of Colloidal $Cu_{2-x}S$ Nanoparticles. $Cu_{2-x}S$ NPs were synthesized using a slightly modified standard procedure.[35] An atmosphere of N_2 or vacuum was provided with the standard Schlenk line techniques. OLA (30 mL) and $CuCl_2{\cdot}2H_2O$ (1.704 g) were loaded into a 50 mL three-necked flask equipped with an evaporator trap, thermometer adapter, rubber septum, and stir bar. The solution was stirred under vacuum for 20 min at room temperature and for 1 h at 120 °C to remove any impurities. The reaction vessel was switched to N_2 atmosphere and heated to 200 °C for 1 h. The color turned transparent yellow-green when the solution temperature reached 200 °C. The solution was held for 30 min at 200 °C and then cooled to 180 °C. The TBDS solution (4 mL) was quickly injected by a syringe into the reaction vessel, and the reaction was allowed to continue for 1 h. After the reaction, the heating mantle was removed, and the reaction vessel was cooled under 40 °C. The precipitate was collected by centrifugation and washed three times with hexane/acetone (∼1:3 v/v) at 5000 rpm for 5 min. The NPs (pristine $Cu_{2-x}S$ NPs) were dispersed and stored in hexane.

2.3. Ligand Treatment/Washing and Recovery Procedures. The "ligand treatment process" involved the following steps:

1 Sonication was performed using an ultrasonicator for 15 min after adding various amounts of OLA (1.5 to 9 mmol) to the pristine $Cu_{2-x}S$ NP solution at a concentration of 0.01 to 0.5 g/L contained in a conical tube.
2 The OLA/NP solution was cleaned by adding hexane/acetone (∼1:3 v/v) and then centrifuging for 5 min at 5000 rpm.
3 The powder was redispersed in hexane to a concentration of 0.01 to 0.5 g/L for preparing a ligand-treated NP solution after the precipitate was completely dried to exclude the influence of organic solvent.
4 The "washing process" was performed using a pristine NP solution. Pristine NPs with the NP concentration of 0.01 to 0.5 g/L were washed twice by centrifugation at 5000 rpm for 5 min. The precipitate was redissolved in hexane to prepare a washed NP solution.

https://doi.org/10.1021/acsomega.2c04366
ACS Omega 2022, 7, 41021−41032

The "recovery process" was performed from the washed NP solution with a concentration of 0.5 g/L. OLAM (~9 mmol) was used for ligand treatment, followed by centrifugation (5000 rpm, 5 min).

2.4. Fabrication of the Nanoparticle Film through the EPD Process. Doped Si wafers (P type, thickness = 525 ± 25 μm, 1.5 × 1.5 cm^2) were attached to a pair of stainless-steel plates (positive and negative electrodes); the gap between the two electrodes was fixed at 5 mm. The substrate was cleaned in acetone with ultrasonication for removal of surface contaminants. Then, the prepared NP solution (concentration of 0.01 to 0.5 g/L) was placed in a tall glass beaker. A pair of electrodes was inserted into the NP solution to cover a deposition area of 1.5 cm^2 and a DC voltage (~500 V) was applied to the plates. In all deposition processes, the potential was supplied through a Keithley 6517B electrometer, while the deposition current was collected using the 6517A measurement computer software. It should be as isolated from ambient vibration and noise as possible when an EPD current of ~nA level is detected. The potential was maintained at different deposition times, and the dark brown solution became transparent because its NP concentration decreased with the increasing deposition time, whereas the NPs were removed from the solution. The potential was turned off when the deposition time was over, and the plates were pulled from the EPD solution to air for drying. The NP-coated substrate was carefully removed from the back plate and further analysis was performed to characterize the samples.

2.5. Materials Characterization. Field-emission scanning electron microscopy (SEM) and energy-dispersive spectrometry (EDS) analyses were performed using a Carl Zeiss SIGMA microscope. X-ray diffraction (XRD) patterns were collected using an AXS New D8 Advance diffractometer (Bruker) with a Cu Kα radiation source and a Lynxeye line detector. The X-ray photoelectron spectroscopy (XPS) analysis was performed on a K-alpha + spectrometer (Thermo Fisher Scientific) using an Al K-alpha source. Zeta potential measurements were performed using a Malvern Zetasizer Pro (Malvern Instruments) with a universal dip cell kit (palladium electrodes with 2 mm spacing) for the non-aqueous system. Four-point probe measurements were performed using a CMT-SR2000N instrument (Advanced Instruments Technology).

3. RESULTS AND DISCUSSION

EPD was adopted to develop well-controlled colloidal NP films; EPD can provide rigid contact between the NPs and the substrate, in addition to providing the tunability of the film morphology. Colloidal $Cu_{2-x}S$ NPs were selected as ideal target particles for a non-polar solvent-based EPD system because they can be dispersed in hexane and readily deposited on a charged substrate during EPD.[9,20,32] For the EPD experiments, quasi-spherical $Cu_{2-x}S$ NPs were synthesized with a narrow size distribution of ~40 nm (Figure 1a). $Cu_{2-x}S$ with copper vacancies exhibit stoichiometry-dependent band gap properties, localized surface plasmon resonance effects, high free-carrier density, and unique optoelectrical properties.[36,37] At the nanoscale, the high interparticle coupling strength and long-range order can be easily realized from the monodispersed NPs.[12] Thus, the synthesized $Cu_{2-x}S$ NPs are advantageous for producing high-density NP films with EPD for use in relevant applications. The XRD patterns (Figure 1c) of the $Cu_{2-x}S$ NPs confirm that the NPs are well matched with the roxbyite phase ($Cu_{1.81}S$), which is unusual in bulk but readily synthesized in colloidal NPs.[38] The EPD is performed under a typical setup

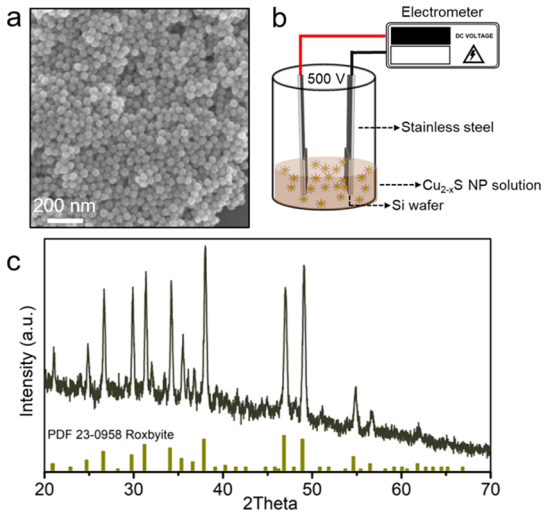

Figure 1. Characterization and fabrication of $Cu_{2-x}S$ NPs: (a) SEM image of NPs; (b) schematic EPD setup; and (c) XRD pattern of NPs (green bars correspond to the roxbyite reference (JCPDS #23-0958)).

(Figure 1b) using $Cu_{2-x}S$ NPs with various NP concentrations from 0.01 to 0.5 g/L.

EPD does not depend on the solvent evaporation unlike drop-casting or the self-assembly of colloidal NPs, and therefore, controlling the assembly of target NPs through EPD parameter control is easy.[39] Among the various EPD factors, the net charge state of the NPs determines the direction and velocity of the particle toward the opposite charged electrodes under an electric field induced by a constant DC voltage. The surfactant ligand coverage on colloidal NPs affects charge formation by serving as an interparticle interaction between the surrounding elements such as ligands and solvents.[40,41] The ligand engineering procedures such as "washing" and "treatment" were performed in our experiments to control the surfactant ligand concentration of the $Cu_{2-x}S$ NPs efficiently.[28,29] Pristine, washed, and ligand-treated NPs were prepared as three types of $Cu_{2-x}S$ NP samples after the ligand control processes. Then, XPS analysis was conducted to verify the change in the amount of surfactant ligands in each NP sample. Pristine NPs were prepared from the as-synthesized NPs with an NP concentration of 0.5 g/L. Ligand-treated NPs were prepared by adding a surfactant ligand (3 mmol) to pristine NPs (0.5 g/L), followed by washing and redispersion in hexane for the same NP concentration of 0.5 g/L. Washed NPs were obtained by adding acetone to the pristine NPs (0.5 g/L), followed by washing once, and redispersing in hexane for the same NP concentration. Finally, the pristine, washed, and ligand-treated NPs were processed into NP films via EPD at 500 V for 800 s on Si wafer substrates (Figure S1a). The change in the amount of surfactant ligands on the NP can be inferred by comparing element signals from the three NP film samples because the OLA ($C_{18}H_{35}NH_2$) ligand on the $Cu_{2-x}S$ NP surfaces was detected as C and N element signals. The precipitation/redispersion of washing reduces the total amount of the surfactant ligand in the final NPs compared to that in the pristine NPs; this is attributed to the partial removal of the ligand from the NP solution. Compared to the *C* and *N* at. % of the pristine NP film, the elemental composition obtained from the washed NP film showed a reduced amount of *C* and *N* because of the partial removal (Table 1). In contrast, the ligand-treated NP film showed significantly increased amounts of *C* and *N*

https://doi.org/10.1021/acsomega.2c04366
ACS Omega 2022, 7, 41021−41032

Table 1. Comparison of Surface Elemental Composition (at. %) Increase/Decrease based on the XPS Analysis of the NP Film Samples: Pristine NP Film, Washed NP Film, and Treated NP Film

at. %	*C* (vs pristine NP film)	*N* (vs pristine NP film)
washed NP film	−2.33	−0.43
treated NP film	+33.28	+1.26

compared to those of the pristine NP sample because of the increased amount of OLA on the NP.

Different amounts of surfactant ligands in each NP sample resulted in changes in the surface charge state, which led to different NP depositions during EPD. The NP charge state was identified by applying the pristine and treated NPs with high dispersibility to the EPD experiment; this was performed by confirming the electrodes where the NPs were deposited among positively and negatively charged substrates. Most pristine NPs are deposited onto the positively charged substrate, and they develop a uniform NP film after EPD (Figure 2a, left panel). Only a few pristine NPs are fabricated, and they form several domains on the negatively charged substrate (Figure 2a, right panel). The differences in the surface morphologies of the pristine NP films suggested that the dominant net charge of the pristine NPs was negative. In contrast to the deposition results of the EPD with the pristine NPs, a highly packed NP film is dominantly fabricated on the negatively charged substrate when the treated NPs are used (Figure 2b, right panel). Only a few NP domains with sizes of ∼300 nm are deposited on the positively charged substrate from the treated NPs (Figure 2b, left panel). Interestingly, several strains are detected on the positively charged substrate (white arrows in Figure 2b, left panel). In the ligand treatment process, the washing procedure was performed to remove excess ligands (unadsorbed ligands dispersed in an NP solution). However, the presence of the remaining ligands in the treated NP solution was inferred from several stains on the substrate.

Elemental mapping images of the pristine and treated NP films for S and Cu are shown in Figure 2c,d, respectively. The low contrast difference in both mapping images suggests that the NP film samples have a highly uniform surface and dense NP packing density over a wide range of substrate areas. Furthermore, low-magnification SEM images of the cross sections (Figure 2e,f) and top views (Figures S1c,d) for both NP film samples demonstrate that crack-free NP films with a thickness of approximately 4 μm are well fabricated.

The surface morphology analysis results of the NP film samples indicate that an increase in the amount of ligand in the NP solution does not significantly affect the film quality of the uniform EPD product. The opposite deposition direction of the NP samples before and after the ligand engineering procedure illustrates that the net charge of the colloidal NPs can be changed from negative to positive depending on the ligand amount in the NP solution. The zeta potential measurements were used to determine the net charge states of the pristine and treated NPs (Figure S1b), which can be considered an indicator of NP movements between the two charged substrates during the EPD. The zeta potential of the pristine NP sample showed a negative value of −21.81 mV, whereas the ligand-treated NP sample exhibited a shift to a positive value (23.25 mV), which clearly supports the flipped charge phenomenon induced by increasing the amount of surface ligands from the pristine NP

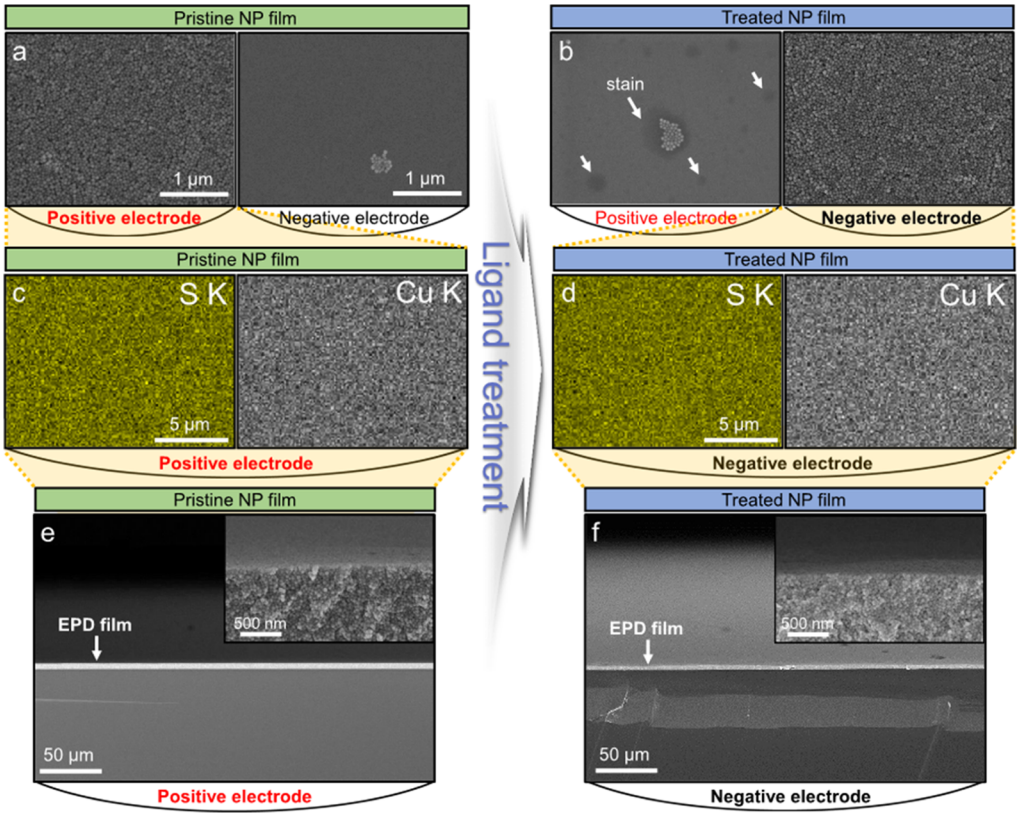

Figure 2. Top-view SEM images of (a) pristine and (b) treated NP films. EDS mapping images of (c) pristine and (d) treated NP film samples. Cross-section SEM images of the NP film samples prepared with (e) pristine and (f) treated NPs.

https://doi.org/10.1021/acsomega.2c04366
ACS Omega 2022, 7, 41021−41032

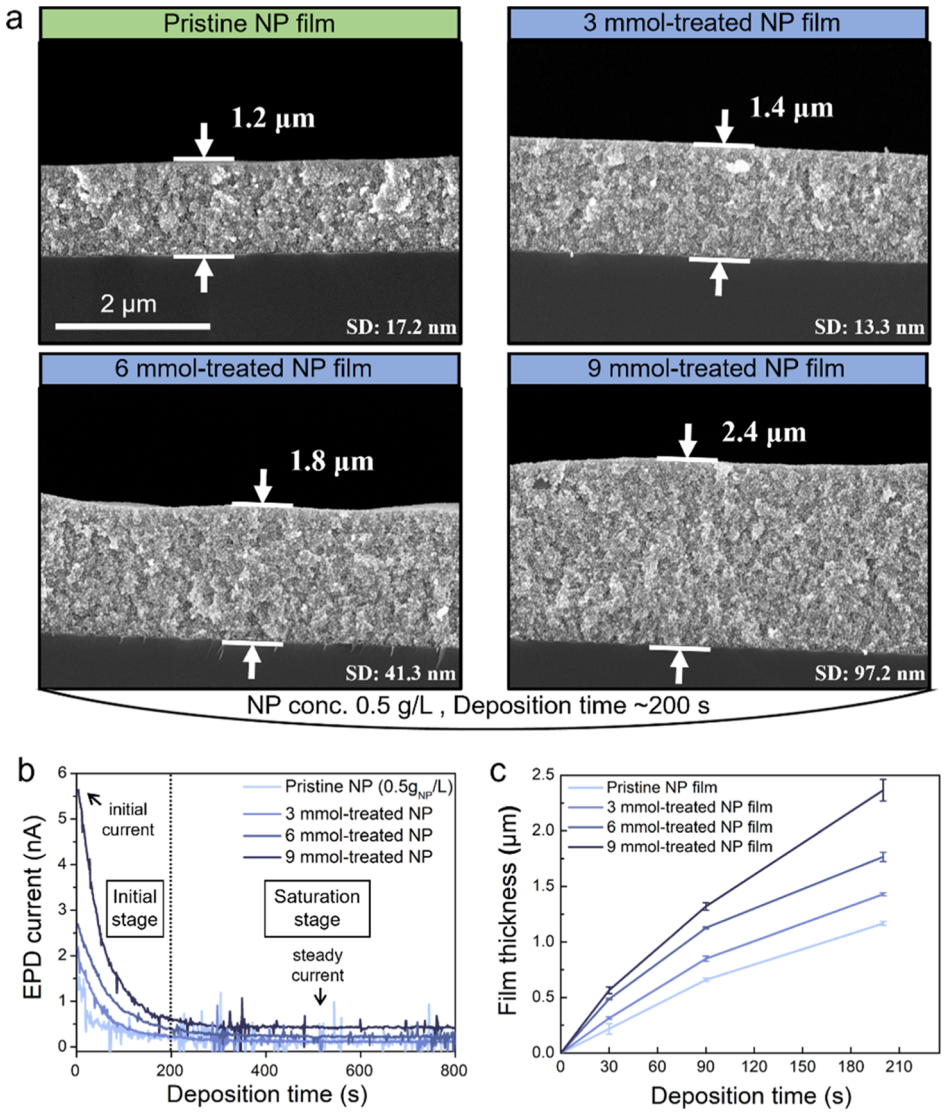

Figure 3. (a) Cross-section SEM images of NP film samples: pristine NP film, 3 mmol-, 6 mmol-, and 9 mmol-treated NP film (SD: standard deviation of the mean thickness). (b) EPD current measurements. (c) Dependence of film-thickness against deposition time within 200 s.

solution. Furthermore, the electric field formed between the parallel substrates by a high voltage (~500 V) provided sufficient force to move the NPs, which contributes to their irreversible deposition onto the substrate with highly packed NP films.

Surfactant ligands in NPs can influence NP assemblies on the substrate through the role of ligands such as the control of interparticle electrostatic repulsion, electrophoretic mobility, and threshold electric field strength for particle movement during EPD.[42−44] For our EPD experiments, different charge formations of OLA-capped $Cu_{2-x}S$ NPs dispersed in hexane were successfully controlled by ligand engineering, which is demonstrated by the film morphology analysis (Figure 2) and zeta potential measurements (Figure S1b). Various NP deposition kinetics can be realized by controlling the amount of the surfactant ligand in the EPD solution. EPD experiments were performed on four types of $Cu_{2-x}S$ NPs with different ligand treatment amounts at an NP concentration of 0.5 g/L. The pristine, 3 mmol-, 6 mmol-, and 9 mmol-treated NPs were assembled into NP films via EPD at 500 V for 200 s. Even after the deposition time of 200 s, all NP solution colors remained opaque brown, which suggests that there are still sufficient NPs in the solutions. The thicknesses of the 3, 6, and 9 mmol-treated NP films were 1.4, 1.8, and 2.4 μm, respectively, which are higher than those of the pristine NP film with a thickness of 1.2 μm (Figure 3a). The surface roughness (standard deviation of the mean thickness) of the NP films increased slightly as the amount of ligand treated in the EPD solution increased, probably due to the different deposition kinetics of the NPs. Through such thickness dependency resulting from different ligand treatments, it was shown that the ligand amount on the NP solution can control the deposition rate in the short period (<200 s) of the EPD.

Another important indicator of deposition kinetics is the EPD current. Colloidal NPs stabilized in non-polar solvents such as hexane and chloroform show low currents (nanoamperes to microamperes) under a high DC voltage (~500 V). A high DC voltage is required to produce a high-quality NP film; however, a stable process is achievable under suppressed side electrochemical reactions because of the low current flow of organic non-polar solvents. The NP movement is affected by a typical phenomenon if a constant voltage is applied to a pair of

https://doi.org/10.1021/acsomega.2c04366
ACS Omega 2022, 7, 41021−41032

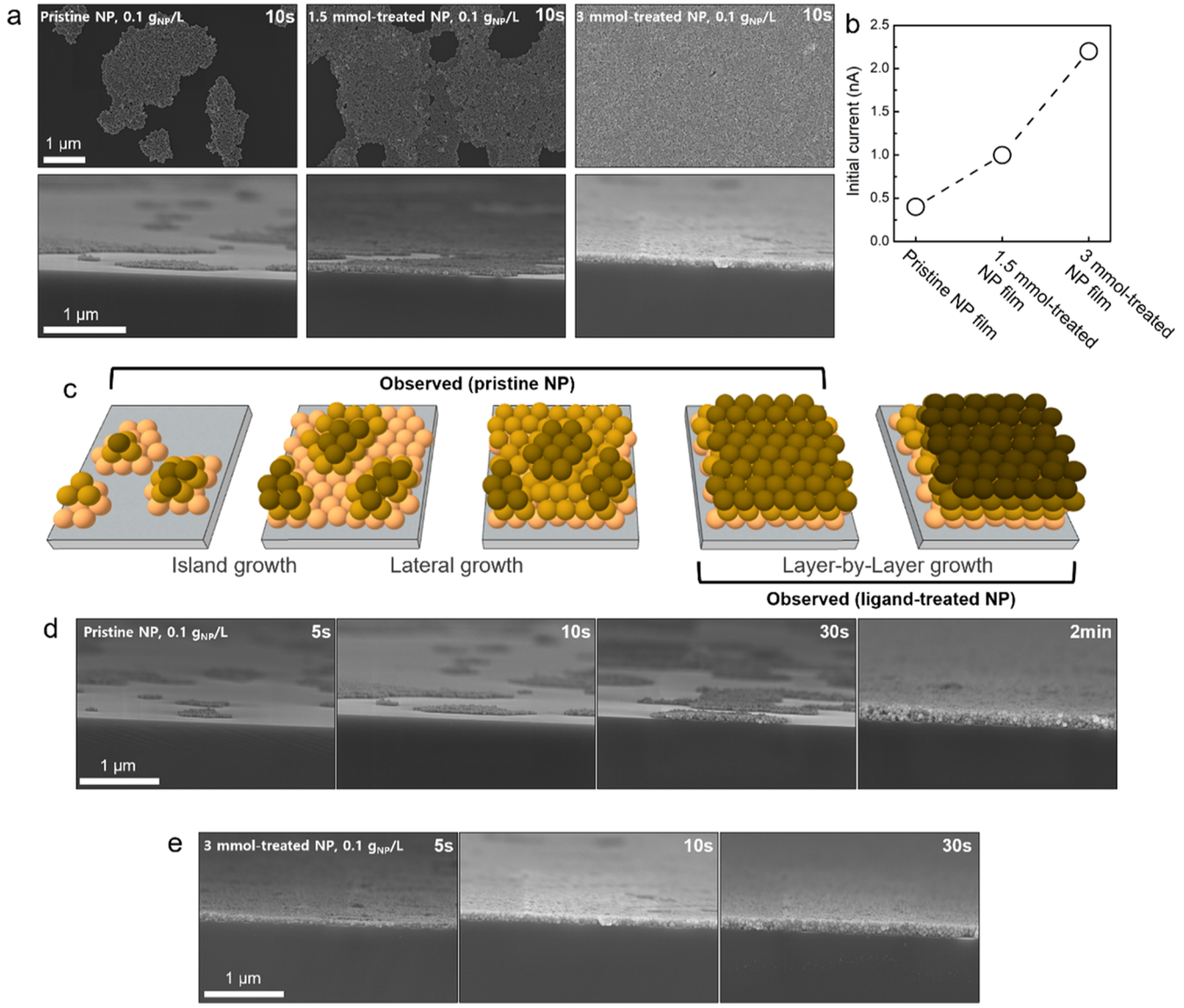

Figure 4. Dependence of the NP film growth mechanism against ligand treatment amounts for the NP film samples. (a) SEM images and (b) initial EPD currents of the pristine NP film, 1.5 mmol-treated NP film, and 3 mmol-treated NP film. (c) Schematic depicting the change in the NP film growth mechanism depending on the ligand treatment conditions of the colloidal $Cu_{2-x}S$ NPs. Cross-section SEM images of the (d) pristine NP film and (e) 3 mmol-treated NP film samples.

electrodes; this can be represented by an exponential decrease in the EPD current. This typical EPD current decrease can be explained by several mechanisms, which are as follows:[45]

1 Deposited materials on the electrode induce capacitive and resistive voltage drops during EPD.
2 Remnant charge accumulation on the electrodes caused by incomplete charge transfer from the NP to the electrode.
3 Dielectric and resistive properties changed as the concentration of NPs in the solution decreased.

The EPD current, a key indicator for unraveling NP dynamics, was measured in the EPD experiments to analyze such mechanisms (Figure 3b). The initial stage exhibited an exponential decay from the initial current until 200 s under an electric field. The current measured immediately after voltage application is expressed as the "initial current." The "steady currents" are currents that are continuously displayed in the saturation stage. NP films with significantly different thicknesses were obtained within the initial stage of EPD (<200 s), depending on the different ligand treatment amounts with the same NP concentration (Figure 3a). The initial EPD currents of 9 mmol-, 6 mmol-, 3 mmol-treated, and pristine NP films were 5.64, 2.7, 2.2, and 1.25 nA, respectively; these values are consistent with the trend of the film thickness after 200 s deposition (initial stage), which were 9 mmol- (2.4 μm), 6 mmol- (1.8 μm), 3 mmol-treated (1.4 μm), and pristine NP films (1.2 μm). In addition, the 9 mmol-treated NP film grows faster than the other samples during the deposition time of 200 s (Figure 3c), which is in line with the rapid exponential current decrease from the highest initial current (5.64 nA) of the 9 mmol-treated NP film during EPD. A high initial current of the EPD was realized by increasing the amount of ligand in the $Cu_{2-x}S$ solution; this indicated a fast NP deposition rate during the initial EPD stage.

NP film morphologies were analyzed to confirm the NP film growth mechanism during the initial EPD stage. The pristine,

https://doi.org/10.1021/acsomega.2c04366
ACS Omega 2022, 7, 41021−41032

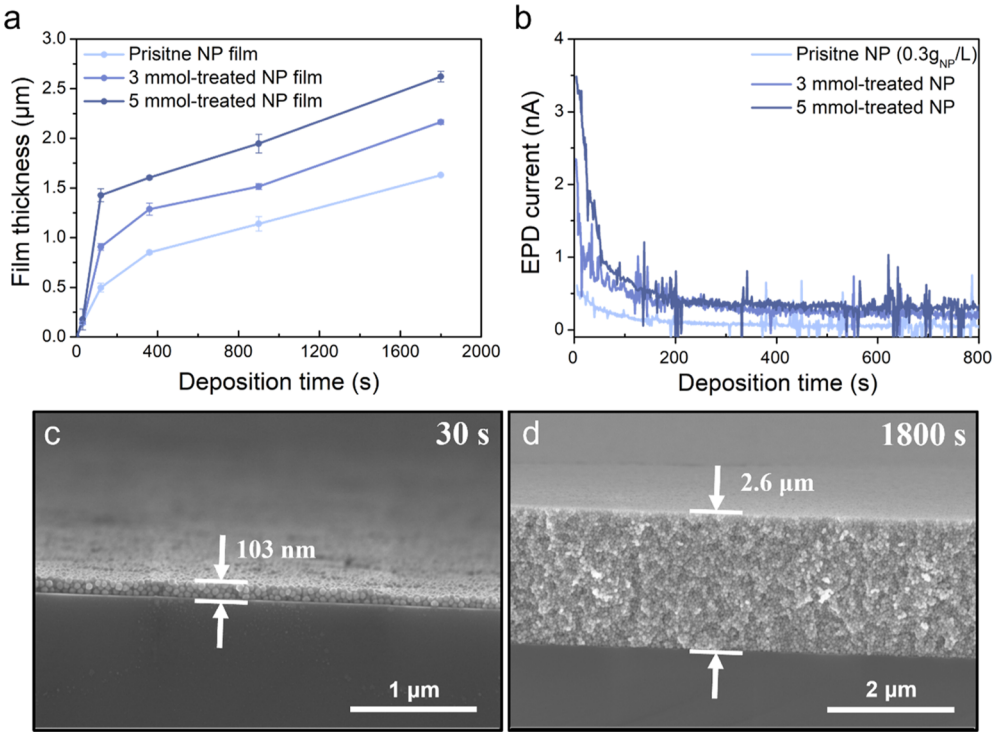

Figure 5. (a) Dependence of film thickness against deposition times for the samples fabricated from pristine, 3, and 5 mmol-treated NP solutions. (b) EPD current measurements. Cross-sectional SEM images of the 5 mmol-treated NP film samples at deposition times of (c) 30 and (d) 1800 s.

1.5 mmol-, and 3 mmol-treated NP films were fabricated from the NP solutions with a concentration of 0.1 g/L (Figure 4a). For the pristine NP film, several NP islands of various sizes were formed on the Si wafer substrate at a deposition time of 10 s (Figure 4a, left panel). The 1.5 mmol-treated NP film showed large NP islands and NP monolayers connecting these domains (Figure 4a, middle panel). In the 3 mmol-treated NP film, NPs were densely deposited and completely covered on the substrate (Figure 4a, right panel). Substrate coverages by the NPs of the pristine NP film, 1.5-treated NP film, and 3 mmol-treated NP film were 19.7, 72.5, and 100%, respectively (Figure S2a), which reflects different deposition kinetics at the same deposition time. Furthermore, the initial currents obtained from the EPD of the pristine NP, 1.5 mmol-, and 3 mmol NPs were measured as 0.4, 1, and 2.2 nA, respectively (Figures 4b and S2b). The improved NP deposition kinetics were characterized by an increased NP coverage and initial currents after ligand engineering. Furthermore, the similar trend for the ligand treatment-dependent deposition kinetics was shown in the EPD experiment with the lowest NP concentration of 0.01 g/L, which presents a faster deposition for higher amounts of ligand treatment (Figure S3).

The deposition time-dependent film growth morphologies are collected from the NP film samples of pristine and 3 mmol-treated NPs during EPD for a systematic analysis of the initial stages of the NP film growth through EPD (Figure 4d,e). A low concentration (0.1 g/L) of EPD solutions were used to track the morphological changes of NP film samples within a short initial EPD period easily; the low concentration limits the total deposit mass and rate of the NP deposition. The typical NP film growth mechanism in our EPD experiments follows the schematic shown in Figure 4c, which indicates that the mechanism is characterized by island formation and the lateral growth of multiple NP islands; furthermore, layer-by-layer (LBL) growth is initiated when approximately three NP layers are formed. The EPD of pristine and ligand-treated NPs follows these typical growth mechanisms with slightly different deposition rates (Figure 4d,e).

First, the island growth of pristine NPs was dominant within the deposition period up to ~10 s (Figure 4d). Then, the lateral growth of multiple NP islands was observed at 30 s filling the voids. The LBL mechanism was initiated by the formation of a multilayered NP film (deposition time of 2 min) with a flat NP film surface when the films formed approximately three NP layers. For the EPD of the 3 mmol-treated NPs, the LBL mechanism is observed even at an initial deposition time of 5 s (Figure 4c,e) because of the fast NP deposition. Ligand-treated NP film samples obtained prior to the deposition time of 5 s may follow the island mechanisms that were observed in the early stage with pristine NPs. Vertical growth by LBL was continued for the 3 mmol-treated NP film at ~30 s of EPD. Such an early emergence of the LBL mechanism for the ligand-treated sample suggests that ligand treatment plays a role similar to that of the deposition time for pristine NPs by controlling deposition kinetics without influencing the deposition mechanism.

Influencing factors for colloidal NP assembly are the combined roles of net charge, dipole moment, coulomb repulsion, and surfactant ligand environment with intervention of external forces such as electric field.[10,30,39] The different environments of surfactant ligands for each treated NP influence the particle-to-particle interactions, leading to different NP movements near the substrate under the electric field. Dominant dipole moment between the NPs may lead to the interface-limited growth that leads to chain growth of the NP assemblies. In contrast, the predominance of coulombic repulsion between nearly equally charged colloidal NPs can induce diffusion-limited growth, which is probably the growth mode supporting our dense $Cu_{2-x}S$ NP film formation.

https://doi.org/10.1021/acsomega.2c04366
ACS Omega 2022, 7, 41021−41032

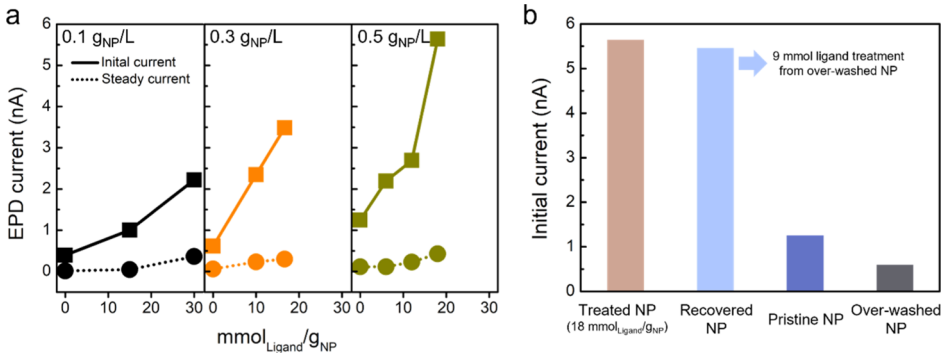

Figure 6. (a) Initial (solid line) and steady currents (dotted line) plotted against the ligand treatment amount per NP amount (0 ~ 30 $mmol_{Ligand}/g_{NP}$) at each NP concentration (0.1, 0.3, and 0.5 g/L). (b) Initial currents for the EPD of the 9 mmol-treated NPs (18 $mmol_{Ligand}/g_{NP}$), recovered NPs (9 mmol ligand treatment from the over-washed NPs), pristine NPs, and over-washed NPs.

The deposit mass of particles and the deposition time have a linear relationship with the EPD.[16] In our experiments, the $Cu_{2-x}S$ NP deposit mass on the substrate represents the NP film thickness with a long deposition time of EPD. The EPD processes are performed with the pristine, 3 mmol-, and 5 mmol-treated NPs (0.3 g/L) throughout the deposition time of 1800 s (Figure 5a). For the initial deposition period (<200 s), the pristine, 3 mmol-, and 5 mmol-treated NP films achieved thicknesses of 0.5, 0.9, and 1.4 μm, respectively. Then, each NP film grew continuously at a similar NP film growth rate (~6×10^{-4} μm/s). Finally, the thicknesses of the pristine, 3 mmol-, and 5 mmol-treated NP films were 1.6, 2.1, and 2.6 μm, respectively. The NP film growth rate before a deposition time of approximately 200 s eventually acted as a factor when determining the final NP film thickness.

The initial EPD currents of the 3 mmol- (2.3 nA) and 5 mmol-treated NP films (3.5 nA) are 4−6 times higher than that of the pristine NP film of 0.6 nA (Figure 5b). Ligand treatments for the NPs significantly control the NP deposition kinetics during the initial period of EPD, and this can be expressed by the increased initial current compared with that during the EPD of the pristine NP film. Indeed, the amount of ligand treatment in the NPs was involved in the control of the NP film growth rate at the initial stage (<200 s); however, it had little effect on NP deposition kinetics during the saturation stage (200−1800 s). The steady currents measured on the saturation stage of the EPD were 0.3 nA (5 mmol-treated NPs), 0.23 nA (3 mmol-treated NPs), and 0.05 nA (pristine NPs), respectively. Although a stable steady current was measured during the saturation stage (Figure 5b), the $Cu_{2-x}S$ NPs were continuously deposited on the substrate at a constant deposition rate (Figure 5a). Cross-sectional SEM images of the 5 mmol-treated NP film samples shown in Figure 5c,d are obtained at deposition times of 30 and 1800 s, respectively. Both samples with film thicknesses of 103 nm and 2.6 μm indicate a highly packed structure with a uniform surface, which can be attributed to the NP film growth occurring through a LBL mechanism during the EPD. For following the LBL growth mechanism during the deposition time from 30 s to 30 min, the irreversible adsorption of NPs on the charged substrate needs to prevail over the two-dimensional physical mobility of the substrate surface,[30] especially with the ligand treatment.

The initial and steady currents of the EPD experiments are summarized in Table S1. The initial and steady current values are shown in Figure 6a, which is plotted against the ligand treatment amount per NP (0−30 $mmol_{Ligand}/g_{NP}$) at all NP concentrations (0.1, 0.3, and 0.5 g/L). All initial and steady currents clearly increased with an increase in the ligand treatment amount per NP. The initial current values obtained from the pristine NP solutions (0 $mmol_{Ligand}/g_{NP}$) of 0.1, 0.3, and 0.5 g/L NP concentrations without ligand engineering treatment were 0.393, 0.612, and 1.247 nA, respectively. The increase in the measured EPD current as the concentration of the clear particle solution increased from 0.1 to 0.5 was likely due to the increased ligand concentration as well as the increased number of particles in the solution. The increase in the initial current as the concentration of the pristine NP solution controlled from 0.1 to 0.5 g/L may be due to the increased ligand concentration as well as the increased number of particles in the solution. For the ligand-engineered NP samples, the initial currents increased at all NP concentrations with an increase in the ligand concentration. Furthermore, the steady current increase of up to 8.7-fold was detected in the pristine NP solution (0 $mmol_{Ligand}/g_{NP}$) when the NP concentrations changed from 0.1 to 0.5 g/L; this indicates that the NP concentration influence the steady current (Figure 6a). Higher steady currents were observed when higher amounts of ligands were used for all three NP concentrations; this indicates that the controlled ligand amounts in the NP solutions contributed to the change in the steady EPD currents, and this does not reflect the NP deposition rates. An increase in the steady current of the ligand-treated NPs (>0 $mmol_{Ligand}/g_{NP}$) compared to that of the pristine NP (0 $mmol_{Ligand}/g_{NP}$) suggests that ligands, especially residual ligands, may affect the steady currents. For solvents without NPs, all currents of the mixture samples prepared by mixing hexane and various amount of OLA ligands showed average values lower than 0.4 nA without a current decay (Figure S4). Residual ligands in the NP solution may primarily contribute to steady currents after the initial current drops exponentially, and this is not representative of the NP deposition rate on the substrate.

For colloidal NPs, excessive washing can result in insufficient surface ligands, and this can lead to the formation of NP aggregates. The over-washed NPs readily form aggregates and quickly sink to the bottom of the beaker during EPD. This gravitational sedimentation of the over-washed NPs is more dominant than the movement of the NPs toward oppositely charged electrodes by the electric field. Such unstable colloidal NPs can be recovered through ligand recovery, which is performed by providing excess OLA ligands to the over-washed NPs. Further understanding of the EPD currents was achieved through such a surface ligand engineering approach. Additional EPD experiments with an NP concentration of 0.5 g/L are

https://doi.org/10.1021/acsomega.2c04366
ACS Omega 2022, 7, 41021−41032

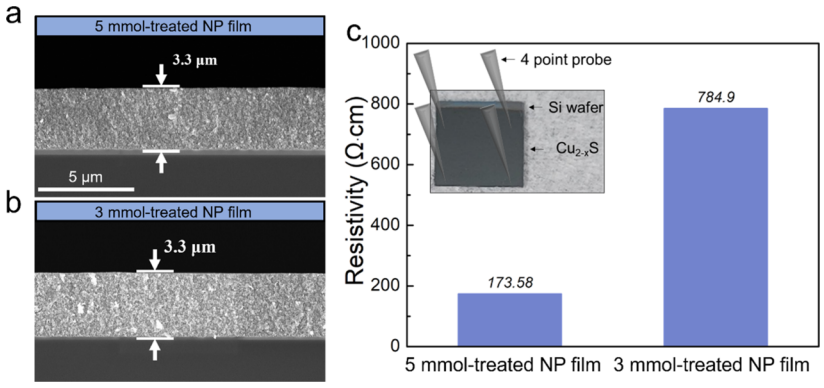

Figure 7. SEM images of the (a) 5 mmol- and (b) 3 mmol-treated NP film samples. (c) Resistivities of the NP film samples obtained by the four-point probe measurement.

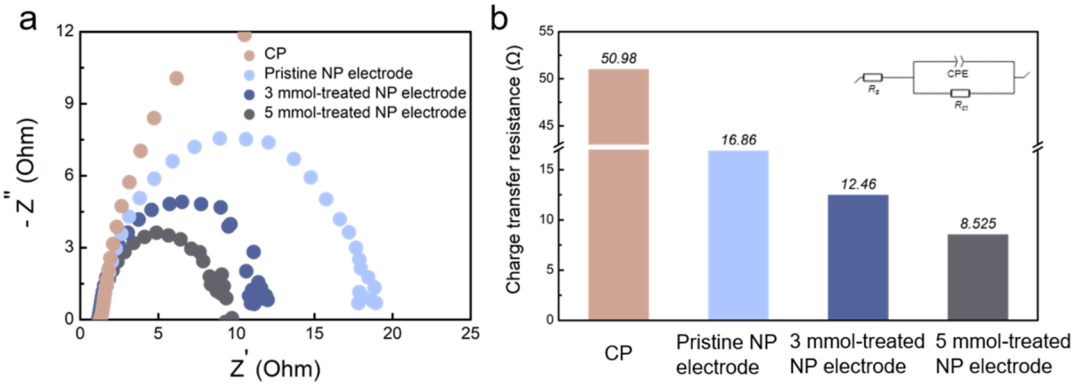

Figure 8. (a) Nyquist plots and (b) charge transfer resistance values of the NP electrode sample.

performed by analyzing the initial current for the samples of pristine, 9 mmol-treated (18 $mmol_{Ligand}/g_{NP}$), over-washed NPs, and recovered NPs (9 mmol ligand treatment from the over-washed NPs) (Figure 6b). The over-washed NPs showed a lower value (0.59 nA) than that of the pristine NPs (1.25 nA), and this indicates that the NP washing step leads to a decrease in the NP deposition kinetics. Furthermore, the initial currents of the recovered NPs and 9 mmol-treated NPs showed similar values of 5.45 and 5.64 nA, respectively, which demonstrates that the deposition kinetics of the recovered NPs can be refreshed at a level similar to that of the 9 mmol-treated NPs from the pristine NPs. Such ligand engineering, even after the over-washed NPs, confirms the crucial role of ligands in tuning the NP deposition kinetics reflected by EPD currents.

The EPD process was applied to the fabrication of nanostructured films to realize the p-type semiconductor characteristics of the $Cu_{2-x}S$ NPs for macroscale devices. The $Cu_{2-x}S$ NP-based film achieves high electron transport properties by constructing a rigid contract film structure.[46] Four-point probe measurements were performed to compare the resistivity of the $Cu_{2-x}S$ NP-based films prepared via EPD with different ligand-treated NP solutions. The 3- and 5 mmol-treated NP film samples showed the same thickness (3.3 μm) on a Si wafer substrate with a ~250 nm oxide layer (Figure 7a,b). This is followed by a chemical treatment, wherein the film samples are immersed in a Na_2S solution (Na_2S of 1 mM in methanol) for 1 min to remove surface organic ligands, which causes charge transfer interference. The 5 mmol-treated NP film showed 173.58 Ω·cm, which is lower than the resistivity of 784.9 Ω·cm obtained from the 3 mmol-treated NP film (Figure 7c). Assembled structures of the NP film samples were maintained even after ligands on the NP surfaces were removed. The low resistivity of the NP film suggests a fast charge transfer between NPs, and this can be attributed to the high adhesion of the NPs to the substrate in the 5 mmol-treated NP film.[9] The high NP deposition kinetics improved the contact between the NPs and substrate, and this led to the improvement of the electrical properties of the $Cu_{2-x}S$ NP-based film.

Furthermore, colloidal $Cu_{2-x}S$ NPs can be collected on porous substrates (e.g., CP and nickel foam) and flat substrates (e.g., Si wafers and metal foils) through EPD. The electrochemical energy conversion electrodes based on a porous CP substrate were fabricated from the pristine and 3 mmol- and 5 mmol-treated NPs, which follow the experimental procedure described in the Supporting Information. The hydrogen evolution reaction (HER) activities of the electrode samples were evaluated using a three-electrode cell in 1 M KOH (Figure S5). The bare CP substrate was inactive, and it showed a high overpotential of 740 mV at 20 mA cm^{-2}. The 5 mmol sample achieved a higher HER activity (531 mV) than the 3 mmol sample (551 mV), and it required a low overpotential to achieve a current density of 20 mA cm^{-2}. The HER activity of the pristine NP electrode was lower than that of the two ligand-treated electrode samples (3 mmol- and 5 mmol-treated NP electrodes), and this indicates that fabricating the electrocatalytic electrode from $Cu_{2-x}S$ NPs prepared by the ligand-treated process via EPD provides the advantage of improving electrocatalytic activity.

The adhesion of the NPs to the substrate can be revealed through the charge transfer resistance (R_{ct}) because it is involved in charge transfer based on the contact between the NP layer and porous CP substrate. A Randle circuit model (inset in Figure 8b)

https://doi.org/10.1021/acsomega.2c04366
ACS Omega 2022, 7, 41021−41032

is used to derive R_{ct} of the Nyquist plots obtained from EIS analysis (Figure 8a) to compare the charge transfer depending on NP adhesion between the electrode samples. The 5 mmol-treated NP electrode has strong adhesion between the particles and the substrate, as indicated by the lowest R_{ct} (8.525 Ω) among the samples (Figure 8b). The fitted R_{ct} values of the CP, pristine NP, and 3 mmol-treated NP electrodes were 50.98, 16.86, and 12.46 Ω, respectively. The high electron transfer of the 5 mmol-treated NP electrode contributed to the fast HER kinetics in an alkaline media.

Furthermore, the inherent electrocatalytic performance of the electrodes may be attributed to the different morphological characteristics of the surface $Cu_{2-x}S$ NP layers. Surface morphologies of electrode samples were compared in the SEM images shown in Figure S6a–d. A thick NP layer of the 5 mmol-treated NP electrode was fabricated on a porous CP substrate (Figure S6c). Several pores were present in the $Cu_{2-x}S$ NP surface (Figure S6d), and this may be attributed to the effect of the complex electric field induced on the porous substrate during the EPD. A 3 mmol-treated NP electrode formed a thinner NP layer with more surface pores than that of the 5 mmol-treated NP electrode (Figure S6b). The difference in the morphology of the deposited NP layer can be attributed to the NP deposition kinetics for the 5 mmol-treated NP electrode being faster than those of the EPD of the 3 mmol-treated NP electrode. Improvements in the deposition kinetics during EPD contributed to an increase in the HER activity of the EPD product because of the formation of rigid catalyst layers. Furthermore, the pristine NP-based electrode exhibited a highly aggregated NP film without full coverage of the substrate, and this may be the main reason for the lowest HER activity among the samples (Figure S6a). Although the prepared $Cu_{2-x}S$ NPs of the roxbyite phase are not ideal HER catalysts,[37,47,48] the positive effect of the EPD with optimized ligand engineering can be clearly demonstrated through a four-point probe measurement and electrochemical analysis.

4. CONCLUSIONS

The colloidal NP deposition behaviors involving surfactant ligands were clarified through the analyses of NP film morphologies, NP deposition mechanisms, and EPD currents. The mechanism of NP deposition and kinetics under the electric field was elucidated from the initial NP deposition to the final stage of film formation, which was affected by the amount of surfactant ligand. The amount of ligand treatment was found to be the key factor determining colloidal $Cu_{2-x}S$ NP charge states and deposition rates for the NP film growth. The high amount of ligand treatment in the pristine NPs led to enhanced NP deposition rates with high initial currents. The deposition time dependence of EPD current is characterized by two main stages. In the initial stage of EPD, ligand engineering affects NP deposition kinetics, which is reflected by the initial currents. Furthermore, in the later stage, similar film growth rates were obtained for NP film samples with different ligand treatment amounts. The typical deposition mechanism of EPD showed three steps of deposition characterized by island formation, lateral growth of multiple NP islands, and LBL growth. The ligand treatment played a role similar to that of the deposition time for the pristine NPs by controlling the deposition kinetics. In the ligand-treated NPs applied as building blocks for the fabrication of nanostructured film devices, the NP film samples achieved low resistivity and fast charge transfer after ligand removal; these were achieved by the formation of rigid NP layers, strong contact of the NP film structure, and strong adhesion between the NPs and substrates. Our deposition process for colloidal NPs can be utilized in the fabrication of high-performance NP-based devices for various applications through the facile ligand engineering technology that can control the surface charge states, deposition kinetics, and deposition mechanisms.

■ ASSOCIATED CONTENT

Supporting Information

The Supporting Information is available free of charge at https://pubs.acs.org/doi/10.1021/acsomega.2c04366.

Experimental section about preparation and electrochemical measurements of the $Cu_{2-x}S$ NP/CP electrode, initial and steady currents collected from the EPD experiments, and detailed supplementary results of materials characterization, EPD currents, and electrochemical analyses (PDF)

■ AUTHOR INFORMATION

Corresponding Author

Don-Hyung Ha − *School of Integrative Engineering, Chung-Ang University, Seoul 06974, Republic of Korea;* orcid.org/0000-0003-4744-6571; Email: dhha@cau.ac.kr

Authors

Yoonsu Park − *School of Integrative Engineering, Chung-Ang University, Seoul 06974, Republic of Korea*

Wooseok Jeong − *School of Integrative Engineering, Chung-Ang University, Seoul 06974, Republic of Korea*

Junhyuk Ahn − *Department of Materials Science and Engineering, Korea University, Seoul 02841, Republic of Korea;* orcid.org/0000-0003-0103-5080

Yun-Kun Hong − *School of Integrative Engineering, Chung-Ang University, Seoul 06974, Republic of Korea*

Eunseo Hwang − *School of Integrative Engineering, Chung-Ang University, Seoul 06974, Republic of Korea*

Minyoung Kim − *School of Integrative Engineering, Chung-Ang University, Seoul 06974, Republic of Korea*

Yun Jae Hwang − *School of Integrative Engineering, Chung-Ang University, Seoul 06974, Republic of Korea*

Soong Ju Oh − *Department of Materials Science and Engineering, Korea University, Seoul 02841, Republic of Korea;* orcid.org/0000-0003-1434-8844

Complete contact information is available at: https://pubs.acs.org/10.1021/acsomega.2c04366

Notes

The authors declare no competing financial interest.

■ ACKNOWLEDGMENTS

This research was supported NRF grant funded by the Ministry of Science and ICT (MSIT) (grant number: 2020R1A5A1018052). This research was supported by the Chung-Ang University Research Scholarship Grants in 2021.

■ REFERENCES

(1) El-Sayed, M. A. Small Is Different: Shape-, Size-, and Composition-Dependent Properties of Some Colloidal Semiconductor Nanocrystals. *Acc. Chem. Res.* **2004**, *37*, 326−333.

(2) Lohse, S. E.; Murphy, C. J. Applications of Colloidal Inorganic Nanoparticles: From Medicine to Energy. *J. Am. Chem. Soc.* **2012**, *134*, 15607−15620.
(3) Murray, C. B.; Kagan, C. R.; Bawendi, M. G. Synthesis and Characterization of Monodisperse Nanocrystals and Close-Packed Nanocrystal Assemblies. *Annu. Rev. Mater. Sci.* **2000**, *30*, 545−610.
(4) Wang, D.; Xie, T.; Li, Y. Nanocrystals: Solution-based synthesis and applications as nanocatalysts. *Nano Res.* **2009**, *2*, 30−46.
(5) Kagan, R.; Lifshitz, E.; Sargent, H.; Talapin, V. Building devices from colloidal quantum dots. *Science* **2016**, *353*, aac5523.
(6) Talapin, D. V.; Lee, J.-S.; Kovalenko, M. V.; Shevchenko, E. V. Prospects of Colloidal Nanocrystals for Electronic and Optoelectronic Applications. *Chem. Rev.* **2010**, *110*, 389−458.
(7) Leatherdale, C. A.; Kagan, C. R.; Morgan, N. Y.; Empedocles, S. A.; Kastner, M. A.; Bawendi, M. G. Photoconductivity in CdSe quantum dot solids. *Phys. Rev. B* **2000**, *62*, 2669−2680.
(8) Ha, D.-H.; Islam, M. A.; Robinson, R. D. Binder-Free and Carbon-Free Nanoparticle Batteries: A Method for Nanoparticle Electrodes without Polymeric Binders or Carbon Black. *Nano Lett.* **2012**, *12*, 5122−5130.
(9) Otelaja, O. O.; Ha, D.-H.; Ly, T.; Zhang, H.; Robinson, R. D. Highly Conductive Cu2−xS Nanoparticle Films through Room-Temperature Processing and an Order of Magnitude Enhancement of Conductivity via Electrophoretic Deposition. *ACS Appl. Mater. Interfaces* **2014**, *6*, 18911−18920.
(10) Krejci, A. J.; Gonzalo-Juan, I.; Dickerson, J. H. Evolution of Ordering in Iron Oxide Nanoparticle Monolayers Using Electrophoretic Deposition. *ACS Appl. Mater. Interfaces* **2011**, *3*, 3611−3615.
(11) Baker, J. L.; Widmer-Cooper, A.; Toney, M. F.; Geissler, P. L.; Alivisatos, A. P. Device-Scale Perpendicular Alignment of Colloidal Nanorods. *Nano Lett.* **2010**, *10*, 195−201.
(12) Hanrath, T. Colloidal nanocrystal quantum dot assemblies as artificial solids. *J. Vac. Sci.* **2012**, *30*, 030802.
(13) Daryakenari, A. A.; Mosallanejad, B.; Zare, E.; Daryakenari, M. A.; Montazeri, A.; Apostoluk, A.; Delaunay, J.-J. Highly efficient electrocatalysts fabricated via electrophoretic deposition for alcohol oxidation, oxygen reduction, hydrogen evolution, and oxygen evolution reactions. *Int. J. Hydrogen Energy* **2021**, *46*, 7263−7283.
(14) Velev, O. D.; Gupta, S. Materials Fabricated by Micro- and Nanoparticle Assembly − The Challenging Path from Science to Engineering. *Adv. Mater.* **2009**, *21*, 1897−1905.
(15) Sarkar, P.; Nicholson, P. S. Electrophoretic Deposition (EPD): Mechanisms, Kinetics, and Application to Ceramics. *J. Am. Ceram. Soc.* **1996**, *79*, 1987−2002.
(16) Besra, L.; Liu, M. A review on fundamentals and applications of electrophoretic deposition (EPD). *Prog. Mater. Sci.* **2007**, *52*, 1−61.
(17) Ye, L.; Wen, K.; Zhang, Z.; Yang, F.; Liang, Y.; Lv, W.; Lin, Y.; Gu, J.; Dickerson, J. H.; He, W. Highly Efficient Materials Assembly Via Electrophoretic Deposition for Electrochemical Energy Conversion and Storage Devices. *Adv. Energy Mater.* **2016**, *6*, 1502018.
(18) Park, Y.; Kim, H.; Lee, T.; Hong, Y.-K.; Jeong, W.; Kim, S.-K.; Ha, D.-H. Design of nanocatalyst for electrode structure: Electrophoretic deposition of iron phosphide nanoparticles to produce a highly active hydrogen evolution reaction catalyst. *Chem. Eng. J.* **2022**, *431*, 133217.
(19) Zhao, J.; Chen, L.; Li, D.; Shi, Z.; Liu, P.; Yao, Z.; Yang, H.; Zou, T.; Zhao, B.; Zhang, X.; et al. Large-area patterning of full-color quantum dot arrays beyond 1000 pixels per inch by selective electrophoretic deposition. *Nat. Commun.* **2021**, *12*, 4603.
(20) Ha, D.-H.; Ly, T.; Caron, J. M.; Zhang, H.; Fritz, K. E.; Robinson, R. D. A General Method for High-Performance Li-Ion Battery Electrodes from Colloidal Nanoparticles without the Introduction of Binders or Conductive-Carbon Additives: The Cases of MnS, Cu2−xS, and Ge. *ACS Appl. Mater. Interfaces* **2015**, *7*, 25053−25060.
(21) Salant, A.; Shalom, M.; Hod, I.; Faust, A.; Zaban, A.; Banin, U. Quantum Dot Sensitized Solar Cells with Improved Efficiency Prepared Using Electrophoretic Deposition. *ACS Nano* **2010**, *4*, 5962−5968.
(22) Kim, B.-J.; Park, J.-S.; Hwang, Y.-J.; Park, J.-S. Characteristics of silver meshes coated with carbon nanotubes via spray-coating and electrophoretic deposition for touch screen panels. *Thin Solid Films* **2015**, *596*, 68−71.
(23) Ferrari, B.; Moreno, R. EPD kinetics: A review. *J. Eur. Ceram. Soc.* **2010**, *30*, 1069−1078.
(24) Ammam, M. Electrophoretic deposition under modulated electric fields: a review. *RSC Adv.* **2012**, *2*, 7633−7646.
(25) Dickerson, J. H.Electrophoretic Deposition of Nanocrystals in Non-polar Solvents. In *Electrophoretic Deposition of Nanomaterials*; Dickerson, J. H., Boccaccini, A. R., Eds.; Springer New York, 2012, pp 131−155.
(26) Černohorský, O.; Grym, J.; Yatskiv, R.; Pham, V. H.; Dickerson, J. H. Insight into Nanoparticle Charging Mechanism in Nonpolar Solvents To Control the Formation of Pt Nanoparticle Monolayers by Electrophoretic Deposition. *ACS Appl. Mater. Interfaces* **2016**, *8*, 19680−19690.
(27) Bass, J. D.; Ai, X.; Bagabas, A.; Rice, P. M.; Topuria, T.; Scott, J. C.; Alharbi, F. H.; Kim, H.-C.; Song, Q.; Miller, R. D. An Efficient and Low-Cost Method for the Purification of Colloidal Nanoparticles. *Angew. Chem., Int. Ed.* **2011**, *50*, 6538−6542.
(28) Islam, M. A.; Xia, Y.; Telesca, D. A.; Steigerwald, M. L.; Herman, I. P. Controlled Electrophoretic Deposition of Smooth and Robust Films of CdSe Nanocrystals. *Chem. Mater.* **2004**, *16*, 49−54.
(29) Jia, S.; Banerjee, S.; Herman, I. P. Mechanism of the Electrophoretic Deposition of CdSe Nanocrystal Films: Influence of the Nanocrystal Surface and Charge. *J. Phys. Chem. C* **2008**, *112*, 162−171.
(30) Singh, A.; English, N. J.; Ryan, K. M. Highly Ordered Nanorod Assemblies Extending over Device Scale Areas and in Controlled Multilayers by Electrophoretic Deposition. *J. Phys. Chem. B* **2013**, *117*, 1608−1615.
(31) Oberdick, S. D.; Majetich, S. A. Electrophoretic Deposition of Iron Oxide Nanoparticles on Templates. *J. Phys. Chem. C* **2013**, *117*, 18709−18718.
(32) Park, Y.; Kang, H.; Jeong, W.; Son, H.; Ha, D.-H. Electrophoretic Deposition of Aged and Charge Controlled Colloidal Copper Sulfide Nanoparticles. *Nanomaterials* **2021**, *11*, 133.
(33) Kang, H.; Park, Y.; Hong, Y.-K.; Yoon, S.; Lee, M.-H.; Ha, D.-H. Solvent-induced charge formation and electrophoretic deposition of colloidal iron oxide nanoparticles. *Surf. Interfaces* **2021**, *22*, 100815.
(34) Hwang, E.; Park, Y.; Kim, J.; Paik, T.; Ha, D.-H. Facile Sulfurization under Ambient Condition with Na2S to Fabricate Nanostructured Copper Sulfide. *Nanomaterials* **2021**, *11*, 2317.
(35) Li, W.; Shavel, A.; Guzman, R.; Rubio-Garcia, J.; Flox, C.; Fan, J.; Cadavid, D.; Ibáñez, M.; Arbiol, J.; Morante, J. R.; et al. Morphology evolution of Cu2−xS nanoparticles: from spheres to dodecahedrons. *Chem. Commun.* **2011**, *47*, 10332−10334.
(36) Sun, S.; Li, P.; Liang, S.; Yang, Z. Diversified copper sulfide (Cu2−xS) micro-/nanostructures: a comprehensive review on synthesis, modifications and applications. *Nanoscale* **2017**, *9*, 11357−11404.
(37) Ren, K.; Yin, P.; Zhou, Y.; Cao, X.; Dong, C.; Cui, L.; Liu, H.; Du, X. Localized Defects on Copper Sulfide Surface for Enhanced Plasmon Resonance and Water Splitting. *Small* **2017**, *13*, 1700867.
(38) Chen, L.; Hu, H.; Chen, Y.; Gao, J.; Li, G. Plasmonic Cu2−xS nanoparticles: a brief introduction of optical properties and applications. *Mater. Adv.* **2021**, *2*, 907−926.
(39) Gill, E.; Liu, P.; Ryan, K. Insights into the Electrophoretic Deposition of Colloidal II-VI Nanorods: Optimization for Vertically and Horizontally Aligned Assemblies. *J. Electrochem. Soc.* **2015**, *162*, D3019−D3024.
(40) Park, Y.-K.; Yoo, S.-H.; Park, S. Assembly of Highly Ordered Nanoparticle Monolayers at a Water/Hexane Interface. *Langmuir* **2007**, *23*, 10505−10510.
(41) Zeng, C.; Chen, Y.; Kirschbaum, K.; Lambright, J.; Jin, R. Emergence of hierarchical structural complexities in nanoparticles and their assembly. *Science* **2016**, *354*, 1580−1584.
(42) Zhang, H.; Wang, D. Controlling the Growth of Charged-Nanoparticle Chains through Interparticle Electrostatic Repulsion. *Angew. Chem., Int. Ed.* **2008**, *47*, 3984−3987.

https://doi.org/10.1021/acsomega.2c04366
ACS Omega 2022, 7, 41021−41032

(43) Streich, C.; Koenen, S.; Lelle, M.; Peneva, K.; Barcikowski, S. Influence of ligands in metal nanoparticle electrophoresis for the fabrication of biofunctional coatings. *Appl. Surf. Sci.* **2015**, *348*, 92−99.
(44) Dillon, A. D.; Mengel, S.; Fafarman, A. T. Influence of Compact, Inorganic Surface Ligands on the Electrophoretic Deposition of Semiconductor Nanocrystals at Low Voltage. *Langmuir* **2018**, *34*, 9598−9605.
(45) Moreno, R.; Ferrari, B. Nanoparticles Dispersion and the Effect of Related Parameters in the EPD Kinetics. *Electrophoretic Deposition of Nanomaterials* **2012**, 73−128.
(46) Li, Z. H.; Egbo, K. O.; Lv, X. H.; Wang, Y.; Yu, K. M.; Liu, C. P. Electronic structure and properties of Cu2-xS thin films: Dependence of phase structures and free-hole concentrations. *Appl. Surf. Sci.* **2022**, *572*, 151530.
(47) Bhat, K. S.; Nagaraja, H. S. Hydrogen evolution reaction at extreme pH conditions of copper sulfide micro-hexagons. *J. Sci.: Adv. Mater. Devices* **2020**, *5*, 361−367.
(48) Fan, M.; Gao, R.; Zou, Y.-C.; Wang, D.; Bai, N.; Li, G.-D.; Zou, X. An efficient nanostructured copper(I) sulfide-based hydrogen evolution electrocatalyst at neutral pH. *Electrochim. Acta* **2016**, *215*, 366−373.

https://doi.org/10.1021/acsomega.2c04366
ACS Omega 2022, 7, 41021−41032